Image fidelity for single-layer and multi-layer silver superlenses

Ciaran P. Moore,[1,*] Matthew D. Arnold,[1,3] Philip J. Bones,[2] and Richard J. Blaikie[1]

[1]*MacDiarmid Institute for Advanced Materials and Nanotechnology, Department of Electrical and Computer Engineering, University of Canterbury, Christchurch, New Zealand*

[2]*Computational Imaging Group, Department of Electrical and Computer Engineering, University of Canterbury, Christchurch, New Zealand*

[3]*Current address: Physics and Advanced Materials, University of Technology Sydney, Sydney, Australia*

**Corresponding author: cmo44@student.canterbury.ac.nz*

Received October 16, 2007; accepted February 5, 2008;
posted February 11, 2008 (Doc. ID 88622); published March 21, 2008

In response to increasing interest in the area of subdiffraction-limited near-field imaging, the performance of several different realizable and theoretical superresolving silver-based lenses is simulated for a variety of different input object profiles. A computationally-efficient T-matrix technique is used to model the lenses, which consist of layers of silver with total width of 40 nm sandwiched between layers of polymethyl methacrylate and silicon dioxide. The lenses are exposed to nonperiodic bright- and dark-slit input patterns, with feature size varied between 1 nm and 2.5 μm. The performance of the lenses is characterized in terms of transfer function, contrast profile, error profile, and input-to-output correlation. It is shown that increasing the number of layers in a lens increases the lens' transmission coefficients at high spatial frequencies; however, this does not always lead to better imaging performance. The main reasons for this are lens-specific resonances that distort features at certain spatial frequencies, and the increased attenuation of the DC component of transmitted images, which reduces image fidelity, particularly for dark-line features. This suggests that, to achieve optimum results, the design of the superresolving lens system should take into account the characteristics of the images that it is expected to transmit.

OCIS codes: 110.3000, 110.3925, 160.3918, 050.6624, 050.1755.

1. INTRODUCTION

After silver-based superresolving lenses were proposed in 2000 [1], working examples were produced near-simultaneously by two separate groups [2,3]. Since then, work has been done to improve the transmission characteristics and resolving power of the superlenses [4,5]. Based on predictions of greatly improved resolution [6,7], one of the approaches taken was to use several very thin, closely spaced layers of silver instead of one, relatively thick layer [5]. This study, initially with a double-layer silver superlens, showed that transmission can be increased by lamination of the silver in the superlens, but improvements in resolving power were not clearly evident due to increased surface roughness in the multilayer system.

For these and other studies there is a need to analyze the theoretical performance, to determine the best lens geometry for subdiffraction-limited imaging and to characterize experimental performance degradation due to system imperfections. To date, this analysis has largely been restricted to lenses' transfer functions [2,7–12], which show the magnitude of light transmitted by the lens over a range of spatial frequencies. Although the transfer functions work well as a rough measure of the abilities of a lens, they do not always reveal the best lens for a given application. Alternatively, the images from discrete or periodic objects have been used to measure performance [2,3,5,8,9]; however, these provide conclusions about a lens' imaging abilities only for the specific objects that the authors have selected.

To illustrate the need for a careful image-quality analysis, examples of the different images that can be obtained from single-layer and multilayer silver superlenses are shown in Fig. 1, with the details of the different lens stacks given in Fig. 2. In Fig. 1, the performance of two different superlenses is compared (one having a single 40 nm thick silver layer and the other having eight 5 nm thick silver laminations) for two different objects: a pair of 20 nm wide *bright* lines with 80 nm center-to-center spacing, and a pair of 20 nm wide *dark* lines with the same spacing (both illuminated with transverse magnetic (TM) polarized, 365 nm wavelength light). These objects have the same information content and the same spatial-frequency spectral extent, differing only in that the dark-line-pair object has a significantly higher DC spatial-frequency component. The imaging of these objects has been carried out using a transfer matrix technique (see Section 2), and line scans of the images of the bright- and dark-line-pair objects are shown in Figs. 1(a) and 1(b), respectively.

For the bright-line-pair object [Fig. 1(a)] the performance of the multilayer superlens is clearly superior to that of the single-layer lens, even though they both have the same silver thickness. This is the case that has been considered previously [6,7], from which a simple conclusion about the superiority of multilayer superlenses

1084-7529/08/040911-8/$15.00

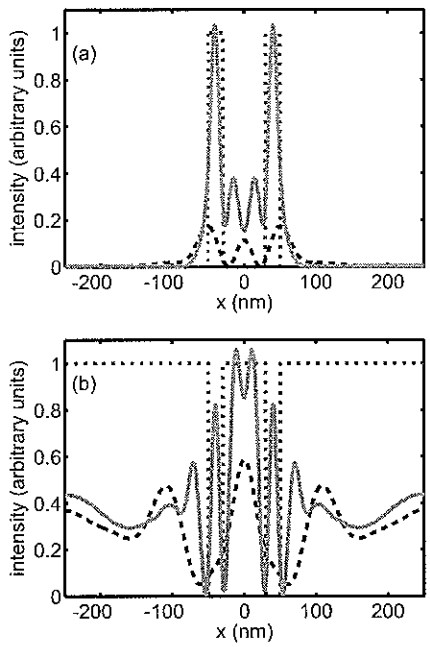

Fig. 1. (Color online) Comparison of 20 nm bright-line-pair versus dark-line-pair images for single-layer and multilayer superlenses. Note that the multilayer lens (solid) outperforms the single-layer lens (dashed) when imaging the bright features (a) but not when imaging the dark features (b).

might be drawn. However, when studying the performance of the same lenses for the dark-line-pair object [Fig. 1(b)] the situation is reversed, with the single-layer lens giving a superior image, and with neither image as sharply defined as the bright-line-pair imaged through the multilayer lens. Hence there is a need to develop a more general set of image classification techniques to complement existing transfer function analysis and example-image comparisons that are usually reported in the literature. To address this shortcoming, quantitative image quality measures have been developed and are presented here, with the aim of providing robust tools that clearly express a lens' strengths and weaknesses in the subdiffraction-limited regime.

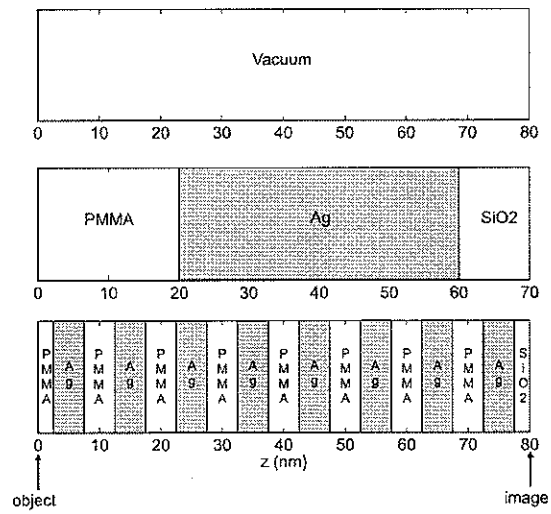

Fig. 2. Lens composition and dimensions. Top: 80 nm vacuum gap used for proximity imaging. Middle: Single-layer silver superlens with 10 nm SiO_2 final layer in accordance with practical experimental conditions [9]. Bottom: Multilayer superlens made up of eight individual 5 nm silver laminations. Total silver thickness is 40 nm, as for the single-layer lens. Input object patterns are applied from the left of the lenses and output images are retrieved from the right, as indicated.

2. METHOD

To test and demonstrate the image-quality metrics considered here, several different practical and theoretical silver-based superlenses were simulated using a matrix-based analytical method, outlined here and fully described elsewhere [8]. Metrics including transfer, contrast, error, and correlation functions were calculated for nonperiodic source patterns exposed to 365 nm (i-line) wavelength light. Results from the superlenses were also compared with those obtained using simple proximity exposure techniques.

T-matrix Analysis. Superlenses were simulated by creating analytical models (2×2 T-matrices) of their component layer interfaces and then taking the matrix product of all of the T-matrices to get the transmission parameters for the entire lens. From [8], the component T-matrices are defined in terms of the dimensions shown in Fig. 3 as follows:

$$\begin{bmatrix} E_x^C \\ E_x^D \end{bmatrix} = \frac{k_z''}{2\epsilon''} \begin{bmatrix} \frac{\epsilon''}{k_z''} + \frac{\epsilon'}{k_z'} & \frac{\epsilon''}{k_z''} - \frac{\epsilon'}{k_z'} \\ \frac{\epsilon''}{k_z''} - \frac{\epsilon'}{k_z'} & \frac{\epsilon''}{k_z''} + \frac{\epsilon'}{k_z'} \end{bmatrix} \begin{bmatrix} E_x^A \\ E_x^B \end{bmatrix} = T(0) \begin{bmatrix} E_x^A \\ E_x^B \end{bmatrix}, \quad (1)$$

where E_x^A represents waves that are incident on the interface, traveling in the positive z direction. For ease of calculation, we set $E_x^A = 1$. Similarly, E_x^D represents waves traveling in the negative z direction, incident on the other side of the interface. We set $E_x^D = 0$. This leaves E_x^B and E_x^C to represent the reflection r and transmission t coefficients of the interface, respectively. These r and t coefficients, which are valid for the $z=0$ plane, are then

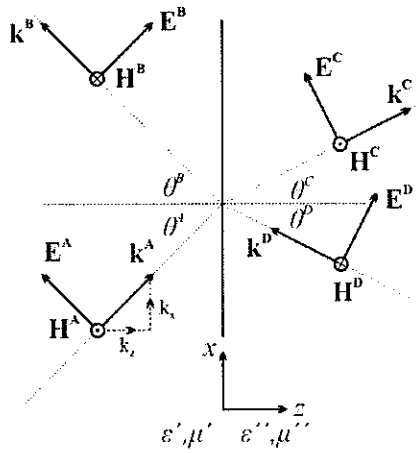

Fig. 3. Component system describing the interaction between transverse magnetic (TM)-polarized waves and a uniform, planar interface [8].

referred to the exit ($z=d$) plane using the phase-transfer matrix

$$T(d)=\begin{bmatrix}\exp(-ik_z''d) & 0\\ 0 & \exp(ik_z''d)\end{bmatrix}T(0)\times\begin{bmatrix}\exp(ik_z'd) & 0\\ 0 & \exp(-ik_z'd)\end{bmatrix}. \quad (2)$$

This process is repeated for each interface in the superlens, creating a stack of T- and phase-transfer matrices. Combining all of the individual T-matrices and their associated phase matrices, the superlens system can be represented by

$$\begin{bmatrix}t\\0\end{bmatrix}=\begin{bmatrix}T_{11} & T_{12}\\ T_{21} & T_{22}\end{bmatrix}\begin{bmatrix}1\\r\end{bmatrix} \quad (3)$$

where T_{xy} are the coefficients of the overall T-matrix at a given spatial frequency. Rearranging for t, we get

$$t=\frac{T_{11}T_{22}-T_{12}T_{21}}{T_{22}}. \quad (4)$$

Hence we have a method of calculating the transmitted intensity t for a given input intensity at a given spatial frequency or wavenumber ($k_x/2\pi$) for different lenses. By extension, a lens' transfer function can be found by collating the values of t at different spatial frequencies.

Although the T-matrix method does not account for interaction between the optical mask used to generate the input intensity profiles and the superlens [9], it does provide a good qualitative estimate of the results generated by full-field simulations [8]. As an aside, work is being undertaken to assess the quantitative effects of these mask–lens interactions, which will be the subject of a separate publication.

The intensity profiles generated by patterns passing through the superlenses were calculated by taking the spatial Fourier transform of an input pattern and point-multiplying it with the lens' transfer function. The inverse Fourier transform of the result gave an output amplitude profile, which was then squared to give the desired intensity profile. A fast Fourier transform (FFT) algorithm that assumed that the input patterns repeated themselves indefinitely was used to calculate the required transformations. To simulate nonperiodic structures, the length of the patterns was increased to large values so that periodic effects were minimized. For the simulations of nonperiodic structures presented here, which examined isolated features from 1 nm to 2.5 μm wide, total pattern widths of 10 μm and 30 μm were used. Either 20,000 or 60,000 samples were taken for each pattern, depending on its total width, to give a Nyquist spatial frequency resolution of 1 nm^{-1}. This allowed for frequency-domain simulations of $k_x/2\pi$ up to 1000 μm^{-1}.

3. IMAGE METRICS

Several figures of merit were considered for classifying and evaluating the performance of different superlenses. Frequency-domain transfer functions were studied to gain an understanding of the range of possible spatial frequency components that a lens could be expected to transmit, while spatial-domain output contrast profiles were used to evaluate the suitability of images produced by superlenses for photolithography applications. Finally, an error function and correlation coefficients were used to evaluate image fidelity to the original input patterns.

A. Transfer Function

The first indicator considered was a lens' transfer function, which is by far the most common imaging metric presented in the literature to date [3,6–12]. This figure of merit makes it easy to see what happens to individual spatial frequency components as they pass through a lens, and hence gives an indication of the minimum feature size that can be transmitted through a lens for a given loss in intensity. Figure 4 shows the simulated transfer functions for two different realizable superlenses—one with only a single 40 nm thick silver layer and the other with eight 5 nm thick silver layers (the cases compared in Fig. 1)—as well as a conventional 80 nm vacuum gap, as shown in Fig. 2. Both superlenses are sandwiched between layers of polymethyl methacrylate (PMMA) and silicon dioxide (SiO_2) to represent typical experimental configurations [8].

The comparison of transfer functions in Fig. 4 highlights the rich spatial-frequency behavior that is present in these systems. By looking at the performance for high spatial frequencies the multilayer lens gives a significant response to $k_x/2\pi \geq 25$ μm^{-1}, corresponding to image features at a scale below 40 nm—a truly impressive performance that would be wonderful to have in practical imaging systems using visible light. This multilayer lens also responds better to these high spatial frequency components than either of the other lenses. However, the performance around and below the diffraction limit (~2.7 μm^{-1} to 4 μm^{-1}) is rather complex, exhibiting a resonant response for the superlenses and differing greatly from system to system. This can have significant impacts on image quality, as illustrated in Fig. 1, which provides motivation for studying additional imaging metrics.

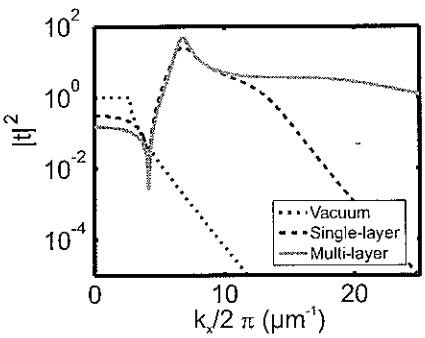

Fig. 4. (Color online) Transfer functions for single-layer and multilayer superlenses and an 80 nm vacuum gap. The single-layer lens is 40 nm thick, sandwiched between PMMA and SiO_2 spacers, whereas the multilayer lens consists of eight 5 nm thick silver laminations (separated by 5 nm) with the same PMMA and SiO_2 outer layers.

B. Contrast

One of the most important image qualities is contrast, which needs to be as high as possible for an image to be of use in a microscopy or lithography process [13]. Accordingly, the Michelson contrast C_M of an intensity profile or image is defined as [14]

$$C_M = \frac{I_{max} - I_{min}}{I_{max} + I_{min}}, \tag{5}$$

where I_{min} and I_{max} are the extreme intensities of the image's electric field, as illustrated in Fig. 5.

These contrast profiles (which evaluate output images independently of the input profiles that are used to make them) can be combined with simple heuristics based on the locations of the intensity extrema in the input profiles to give a pseudocontrast measurement that measures both the suitability of an image for lithography and the fidelity of that image to the original. The need for such a metric is illustrated by Fig. 5, where an output profile with high contrast (C_M=0.998) is shown to be a poor representation of the 75 nm wide single-dark-line object because of the extensive ringing that is induced outside the spatial extent of this dark-line image. Provided the input pattern is relatively simple and largely nonzero, the following definition of pseudocontrast can be used,

$$C_{pseudo} = \frac{I_{DC} - I_{dark}}{I_{DC} + I_{dark}} \tag{6a}$$

where I_{dc} represents the mean or DC intensity of the output and I_{dark} represents the output intensity value corresponding to the location of the minimum intensity in a dark-line or dark-point input profile, as illustrated in Fig. 5. If a bright-line input profile is used then I_{bright} is used in place of I_{dark}, and the definition of pseudocontrast is rewritten as

$$C_{pseudo} = \frac{I_{bright} - I_{DC}}{I_{DC} + I_{bright}}. \tag{6b}$$

For the example shown in Fig. 5, the pseudocontrast is only C_{pseudo}=−0.309, giving a clear indication that the image is distorted relative to the input pattern. The negative value also shows that a form of image reversal (or even frequency doubling) has taken place, as the intensity at the image center (which should be at a minimum) is greater than the background intensity. Note that pseudocontrast is not sensitive to ringing in the image; instead, it is affected only by distortion of the extreme intensity value and DC component of the image.

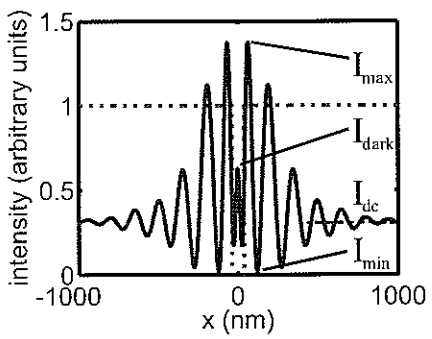

Fig. 5. (Color online) Input (dashed) and output (solid) intensity profiles for a 75 nm feature imaged through a 20:40:10 nm PMMA:Ag:SiO_2 realizable superlens. The definitions for the maximum intensity I_{max}, minimum intensity I_{min}, background intensity I_{dc}, and the intensity at the center of the dark-line feature in the object I_{dark} are shown for use in the contrast and pseudocontrast calculations.

C. Error (Cost)

While Michelson contrast profiles give a good indication of the relative intensities of extrema in the output profile, they do not show how closely the locations of the output extrema match the locations of the input extrema. In other words, they cannot detect image inversion, displacement, or frequency doubling. Modifying the definition of the Michelson contrast to pseudocontrast [Eq. (6a) and (6b)] is a suitable workaround for relatively simple, nonperiodic profiles, but is not practical for complex source images. Even for a single bright slit on an otherwise dark background, the fact that the profile does not have a DC offset means that the contrast profiles become meaningless. Furthermore, the pseudocontrast profiles are very sensitive to high frequency oscillations in the output intensity profiles, which can lead to inaccuracies that are especially noticeable at low spatial frequencies. This is illustrated in Fig. 6(a), which shows the variation in the pseudocontrast profile for dark-line-pair images [e.g., Fig. 6(b)] as the linewidth and line spacing are varied. While the pseudocontrast figure of merit is high (and positive) for linewidths greater than 1000 nm, below this limit oscillations caused by ringing in the image are seen throughout the profile, an example of which is shown in Fig. 6(b). This demonstrates the need for a more robust figure of merit, preferably one that also takes into account the similarity of the input and output profiles.

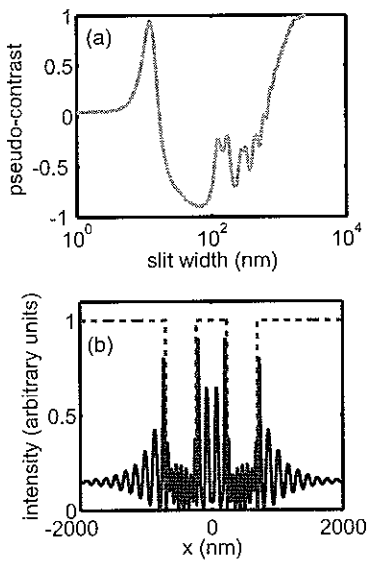

Fig. 6. (Color online) (a) Pseudocontrast profile for a dual dark-slit pattern exposed to a multilayer realizable superlens. Note prevalent ripples between 100 nm and 1 μm. (b) Input (dashed) and output (solid) intensity profiles for a 465 nm dual dark-slit pattern imaged through such a lens.

One such metric is the error H introduced into the image by the lens. Defined by

$$H = \int [as(x) - i(x)]^2 \mathrm{d}x, \tag{7}$$

H is a cost function that gives a comparison between source $s(x)$ and image $i(x)$ profiles by accounting for the attenuation in the resultant profile's DC term using a scale factor a.

By minimizing H with respect to a, we arrive at a determinable expression for the error introduced by the lens:

$$\frac{\mathrm{d}H}{\mathrm{d}a} = \int 2s(x)[as(x) - i(x)]\mathrm{d}x = 0. \tag{8}$$

$$\therefore a = \frac{\int [s(x)i(x)]\mathrm{d}x}{\int s(x)^2 \mathrm{d}x}. \tag{9}$$

Hence,

$$H = \int \left\{ \frac{\int [s(x)i(x)]\mathrm{d}x}{\int [s(x)^2]\mathrm{d}x} s(x) - i(x) \right\}^2 \mathrm{d}x. \tag{10}$$

For ease and speed of calculation, the integration in Eq. (10) is approximated by summation over the image and source sample points, as follows:

$$H = \sum \left(\frac{\Sigma si}{\Sigma s^2} s - i \right)^2. \tag{11}$$

Finally, the error H is normalized by the image support width to allow comparison between profiles with different feature widths but the same overall length.

D. Correlation

The final metric considered is the correlation coefficient of each input profile and its corresponding output profile for a given lens. Although, strictly speaking, the application of correlation coefficients is limited to continuous, independent, normally distributed random variables [15], they are still useful as a description of the level of distortion introduced to the output profile by a lens. Equation (12) following defines the correlation coefficient $r_{s,i}$ for an input profile s and its output profile i [16]:

$$r_{s,i} = \frac{\mathrm{cov}_{s,i}}{\sigma_s \sigma_i}, \tag{12}$$

where σ_s and σ_i are the standard deviations of the intensities of the input and output profiles, respectively, and $\mathrm{cov}_{s,i}$ is their covariance.

The two new (for superlens analysis) image metrics, error and correlation, are used here to compare the performance of a number of superlens systems for a range of different image types, to learn what additional insights into image performance and fidelity can be obtained.

4. RESULTS

Transfer, contrast, error, and correlation metrics were calculated for two different superlenses and a vacuum gap, the composition and dimensions of which are given in Fig. 2. The lenses were exposed to four different, nonperiodic input pattern profile types. These are shown in Fig. 7, and are: a single, bright slit on an otherwise dark background; a single dark slit on a bright background; two bright slits on a dark background, and two dark slits on a bright background. Total pattern width was set at 10 μm for the single-slit patterns, whereas 30 μm was used for the dual-slit patterns because of their larger overall feature size. Slit widths were varied between 1 nm and 2.5 μm. The space between adjacent slits in the dual-slit profiles was set to be the same width as the slits themselves. Image fidelity varied greatly for each of these profiles (see Fig. 1), showing that the performance of the lenses examined is highly application-specific and that increasing the number of layers in a lens does not always lead to better results.

A. Transfer Function

The transfer functions for the lenses, given in Fig. 4, agree with those of other studies [8], which show that increasing the number of silver layers in a superlens while keeping the total silver thickness constant leads to better transmission at high spatial frequencies. Multilayered superlenses do not always provide the best overall image quality, though. This is often due to poor transmission of the DC component of an image and the introduction of resonances that are not as prominent for single-layered superlenses, both features that are evident in the transfer function plots shown in Fig. 4. As an aside, it should be possible to use the resonances introduced in multilayer lenses to selectively enhance certain features in an image. The useful bandwidth of such lenses would be limited, and the practicality of such an application remains to be seen.

B. Contrast

The lenses' Michelson contrast values were calculated for the dark-slit input profiles shown in Figs. 7(b) and 7(d). The resulting profiles are shown in Fig. 8. As expected, contrast is high for all lenses when the slit width is much

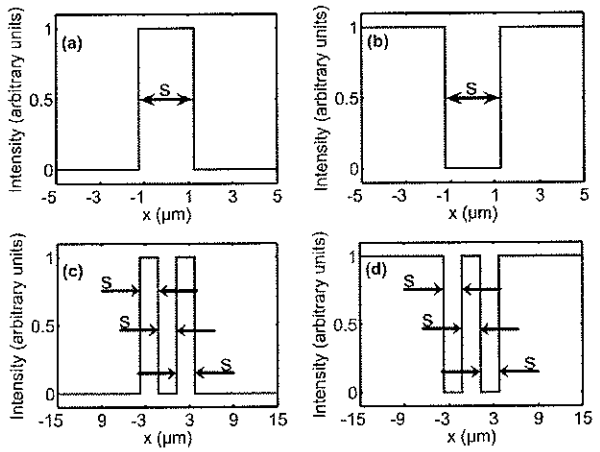

Fig. 7. (Color online) (a) Single bright-, (b) single dark-, (c) dual bright-, and (d) dual dark-slit input intensity patterns used to generate contrast, error, and correlation profiles. Slit width(s) is (are) varied between 1 nm and 2.5 μm.

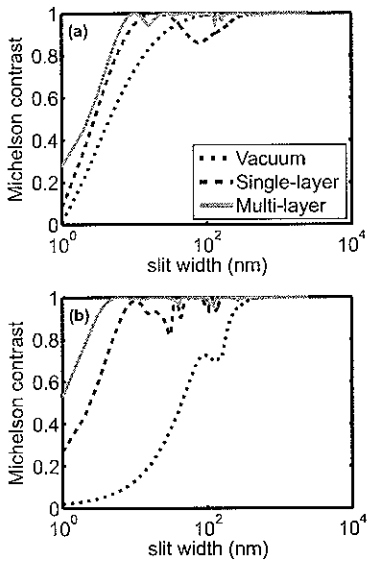

Fig. 8. (Color online) (a) Single and (b) dual dark-slit contrast profiles for single-layer and multilayer superlenses and an 80 nm vacuum gap.

greater than the wavelength of the exposing light (365 nm). In the subwavelength regime, the contrast for the multilayer lens is noticeably higher than for the single-layer lens for dual slit patterns [Fig. 8(b)] due to lower damping in the response of the multilayer lens. This large performance increase is not repeated to the same extent for the single-slit pattern [Fig. 8(a)], as it is not as periodic around its center as its dual-slit cousin. These Michelson contrast results on their own tend to back up the assertion that the multilayer system is superior to its single-layer counterpart; however, this is not supported by simple image examples (e.g., Fig. 1) or other, more sophisticated imaging metrics.

The pseudocontrast profiles for the dark-slit input profiles described in Figs. 7(b) and 7(d) are given in Fig. 9. Here the single-layer lens outperforms the multilayer lens over all slit widths for single-slit patterns, an example of which is shown in Fig. 10. This agrees with other analyses for periodic patterns [10], which attribute the decrease in performance of multilayer lenses to increased suppression of the DC component in their transfer functions. On the other hand, for the dual-slit case [Fig. 9(b)], the multilayer lens has the highest peak pseudocontrast at a slit width of ~12 nm, with both the single-layer and multilayer lenses suffering from image reversal over a large range of slit widths. This is a prime example of how application-specific these lenses are, with a different lens giving the best results for each different input pattern, even if the patterns are largely similar. Michelson and pseudocontrast profiles are not shown for the birght line patterns of Figs. 7(a) and 7(c), as the low DC offset in these profiles reduces the contrast ratio to

$$C \approx \frac{I_{ex} - 0}{I_{ex} + 0} = 1, \tag{13}$$

making the calculations meaningless.

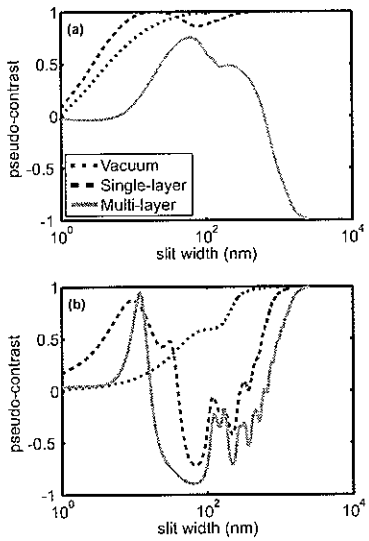

Fig. 9. (Color online) (a) Single and (b) dual dark-slit pseudocontrast profiles for single-layer and multilayer superlenses and an 80 nm vacuum gap.

C. Error

Like the contrast profiles, error functions for all the different image classes studied here (Fig. 11) show interesting characteristics that are not immediately evident in the transfer functions. For instance, there is a matching peak and trough pair in the single dark-slit contrast and error profiles, respectively [Figs. 9(a) and 11(b)], for the PMMA:Ag:SiO_2 lens at 20 nm slit width that is not revealed by other metrics. Furthermore, for slit widths below ~10 nm, the error functions show that there is very little difference in performance between equivalent single-layer and multilayer lenses exposed to bright-slit patterns [Figs. 11(a) and 11(c)]. The insights offered by these error functions are an improvement on the contrast and pseudocontrast profiles, which could not be used on patterns with small or no DC component.

D. Correlation

The correlation coefficients for the dark- and bright-slit profiles defined earlier (Fig. 7) are given in Fig. 12. They highlight an important design consideration, namely, that an image with low distortion (corresponding to a relatively smooth, regular transfer function) is not the same as an image with suitably high luminosity (corresponding

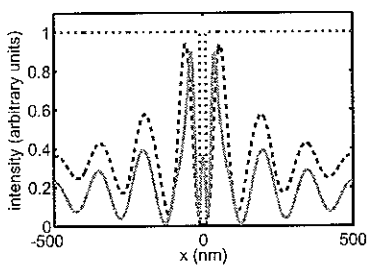

Fig. 10. (Color online) Spatial-domain output for a 20 nm dark slit (dotted) projected through single-layer (dashed) and multilayer (solid) layer realizable superlenses. The pseudocontrast is 0.9997 for the single-layer lens and 0.4033 for the multilayer lens.

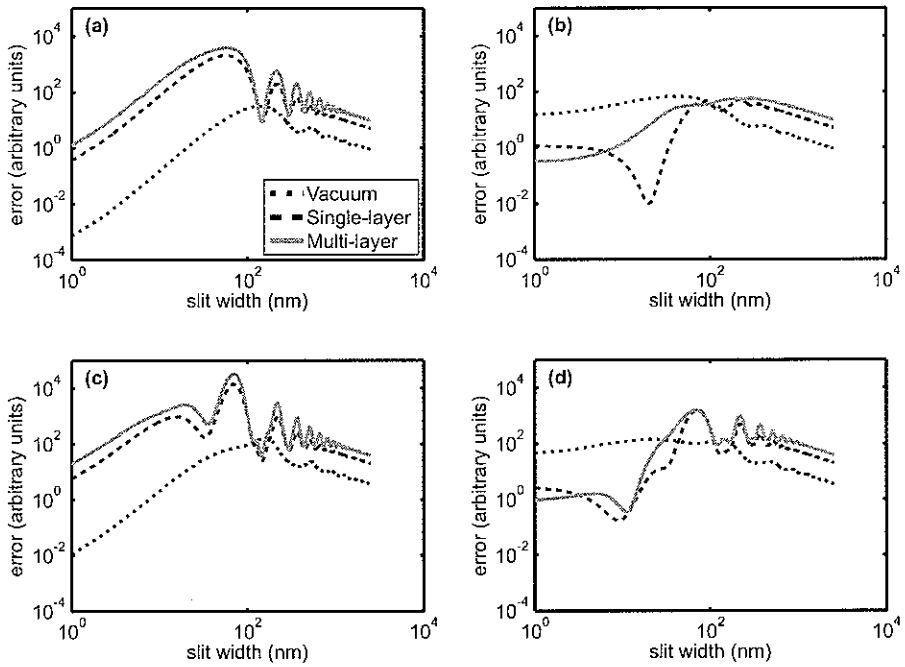

Fig. 11. (Color online) (a) Single bright-, (b) single dark-, (c) dual bright- and (d) dual dark-slit error profiles for single-layer and multilayer superlenses and an 80 nm vacuum gap.

to the area under the transfer function). Although the two are not mutually exclusive, the former often needs to be diminished to improve the latter. Figures 12(b) and 12(d) provide examples of this difference, where the images produced by the proximity 'lens' have higher correlation coefficients (i.e., less distortion) than those produced by the superlenses down to very low feature sizes, but are not very useful due to their extremely low intensities. This perceived mismatch between metrics is due to the fact that the correlation function r fits to a linear model of the data x in the general form

$$r = mx + c. \tag{14}$$

Hence, the correlation coefficient can remain reasonably high despite a low contrast m thanks to the intercept

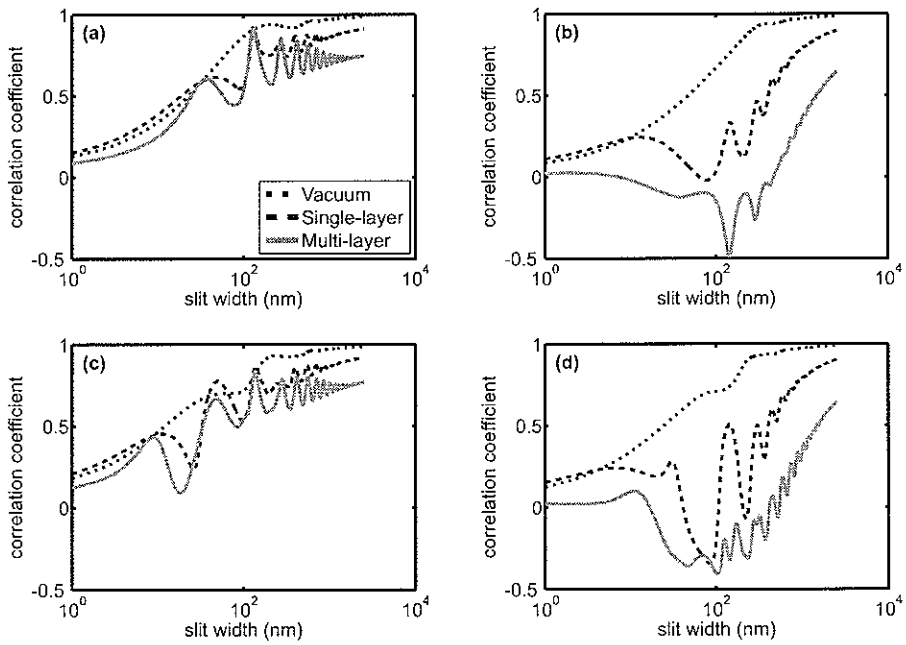

Fig. 12. (Color online) (a) Single bright-, (b) single dark-, (c) dual bright- and (d) dual dark-slit correlation coefficient profiles for single-layer and multilayer superlenses and an 80 nm vacuum gap.

term c. Different models for the correlation, including

$$r = mx, \tag{15}$$

$$r = x, \tag{16}$$

could also be used in future work and may, in fact, prove to be more appropriate.

5. CONCLUSION

New developments in the area of superresolution imaging have given rise to a need for practical, quantifiable image-quality measures that are applicable to a wide range of images. As a result, techniques to measure contrast, error between source and image, and distortion introduced to an image were investigated and applied to several superlenses exposed to one-dimensional luminous intensity profiles. The resulting image characteristics each highlighted different features of the images and showed that, although increasing the number of layers in a superlens increased the transmission coefficients at high spatial frequency, image quality was not necessarily improved. Contrast and error profiles exposed resonances present to differing degrees in different superlenses that can be used selectively either to enhance or damp particular image features. Finally, calculating the correlation coefficients between various input and output profiles showed that the least distorted images are not always the most useful ones. It is hoped that using all of these image metrics in combination will aid in the objective evaluation of the performance of superlensing systems, facilitating further development in the area of subdiffraction-limited imaging.

REFERENCES

1. J. B. Pendry, "Negative refraction makes a perfect lens," Phys. Rev. Lett. **85**, 3966–3969 (2000).
2. D. O. S. Melville and R. J. Blaikie, "Super-resolution imaging through a planar silver lens," Opt. Express **13**, 2127–2134 (2005).
3. N. Fang, H. Lee, C. Sun, and X. Zhang, "Sub-diffraction-limited optical imaging with a silver superlens," Science **308**, 534–537 (2005).
4. S. Durant, Z. Liu, J. M. Steele, and X. Zhang, "Theory of the transmission properties of an optical far-field superlens for imaging beyond the diffraction limit," J. Opt. Soc. Am. B **23**, 2383–2392 (2006).
5. D. O. S. Melville and R. J. Blaikie, "Experimental comparison of resolution and pattern fidelity in single- and double-layer planar lens lithography," J. Opt. Soc. Am. B **23**, 461–467 (2006).
6. E. Shamonina, V. A. Kalinin, K. H. Ringhofer, and L. Solymar, "Imaging, compression and Poynting vector streamlines for negative permittivity materials," Electron. Lett. **37**, 1243–1244 (2001).
7. S. A. Ramakrishna, "Physics of negative refractive index materials," Rep. Prog. Phys. **68**, 449–521 (2005).
8. D. O. S. Melville, "Planar lensing lithography: enhancing the optical near field," Ph.D. thesis (University of Canterbury, New Zealand, 2006).
9. D. O. S. Melville and R. J. Blaikie, "Analysis and optimization of multilayer silver superlenses for near-field optical lithography," Physica B **394**, 197–202 (2007).
10. C. Luo, S. G. Johnson, J. D. Joannopoulos, and J. B. Pendry, "Subwavelength imaging in photonic crystals," Phys. Rev. B **68**, 045115 (2003).
11. N. Fang and X. Zhang, "Imaging properties of a metamaterial superlens," Appl. Phys. Lett. **82**, 161–163 (2003).
12. D. R. Smith, D. Schurig, M. Rosenbluth, S. Schultz, S. A. Ramakrishna, and J. B. Pendry, "Limitations on subdiffraction imaging with a negative refractive index slab," Appl. Phys. Lett. **82**, 1506–1508 (2003).
13. S. J. McNab and R. J. Blaikie, "Contrast in the evanescent near field of $\lambda/20$ period gratings for photolithography," Appl. Opt. **39**, 20–25 (2000).
14. A. A. Michelson, *Studies in Optics* (U. Chicago Press, 1962).
15. H. Lohninger, *Teach/Me Data Analysis* (Springer-Verlag, 1999).
16. H. Abdi, "Coefficients of correlation, alienation and determination," in *Encyclopedia of Measurement and Statistics*, N. Salkind, ed. (Sage, 2007), pp. 158–162.